

ScaleRAFT: Cross-Scale Recurrent All-Pairs Field Transforms for 3D Motion Estimation

Han Ling, Yinghui Sun, Quansen Sun, Zhenwen Ren, and Xian Xu

Abstract—In this paper, we study the problem of estimating the 3D motion of dense pixels from continuous image pairs. Most previous methods are based on mature optical flow baselines and depth values, projecting the 2D motion on pixel planes into 3D space, and further optimizing the results by combining depth-motion-branch and other sub-modules. This stacked framework cannot leverage the complementarity between optical flow and other modules nor escape the dependence on accurate depth information. To address the above challenges, we propose a normalized scene flow framework, ScaleRAFT, based on cross-scale matching. Its core feature is directly matching objects between two frames in 3D scale space, i.e. matching features at the correct location and scale. Unlike previous methods, ScaleRAFT integrates optical flow and deep motion estimation into a unified architecture, allowing the optical flow pipeline and deep motion estimation to promote each other mutually. Moreover, ScaleRAFT estimates motion in the depth direction based on feature matching, breaking away from the dependence on accurate depth information. Experimentally, our method has achieved the best foreground performance so far in motion estimation tasks in driving scenarios, and has significantly improved various downstream 3D tasks.

Index Terms—Motion-in-depth, cross scale, correlation volume, scene flow, optical flow, monocular 3d, time-to-collision.

I. INTRODUCTION

THREE-DIMENSIONAL flow aims to estimate the motion trend of pixel points in a pair of images in 3D space, which is numerically composed of optical flow and motion in the depth directions. It is a long-standing and important problem in computer vision [1]–[12].

Previous Works. Most advanced 3D flow methods are based on mature optical flow pipelines [13]–[17]. They project the pixel flow results estimated by the optical flow pipeline into 3D space through depth values, and add sub-modules such as deep motion branches or rigid optimization to enhance the results further. Although they have achieved remarkable results, their framework highly relies on the optical flow pipeline and input depth values, so defects in the optical flow module or depth value will directly damage the overall performance. There is also a type of 3D flow method [18],

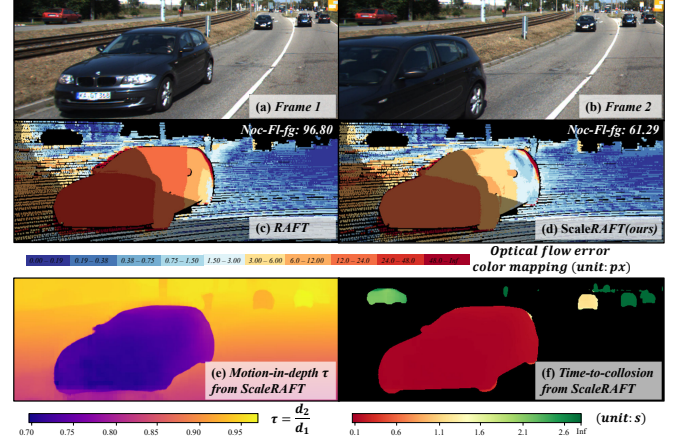


Fig. 1. Tradition matching vs cross-scale matching (ScaleRAFT). From top to bottom are: (a,b) two consecutive frames of input images, (c,d) optical flow error maps based on tradition matching and cross-scale matching, respectively, (e) motion in the depth direction based on ScaleRAFT, (f) The collision time of the foreground targets predicted based on ScaleRAFT. Notice that in (c,d), the foreground error of the baseline method is greatly reduced (96.8→61.29), thanks to cross-scale matching reducing the impact of scale changes on optical flow matching. In addition, CSCV also provides key clues for deep motion, and (e, f) demonstrates its application in 3D visual tasks.

[19] based on monocular images; They regress motion-in-depth (MID) from optical flow or image pairs, resulting in sub-precise and low robustness results. Moreover, they separated the estimated pipelines of optical flow and MID, without utilizing the complementarity between pipelines.

In addition to the problems of the 3D flow framework itself, the optical flow pipeline as its cornerstone also has inherent flaws that have been ignored for a long time. Most optical flow methods [20]–[24] rely on feature-matching techniques, correlating objects in two frames by comparing the correlation between features. However, we found that feature matching in optical flow is limited to the original scale. When an object moves along the camera’s Z-axis (depth direction), its scale change often leads to feature-matching failure. Fig. 3 shows a typical example where, except for the occluded area, the principal errors of the optical flow algorithm are concentrated in the area where scale changes occur, indicating that scale changes are one of the essential reasons for optical flow errors.

Inspiration. The inspiration for solving the above problem comes from the SIFT [25] matching algorithm proposed by Lowe et al. in 2004. They also recognized the impact of scale factors on feature point matching and constructed a scale pyramid to extract scale-invariant features, ultimately achieving stable cross-scale feature point matching. Further,

Han Ling and Quansen Sun are with the School of Nanjing University of Science and Technology, Nanjing, Jiangsu, 210094. Zhenwen Ren is with the School of Southwest University of Science and Technology. Yinghui Sun and Xian xu is with the School of Southeast University. (Corresponding authors: Quansen Sun)

E-mail: 321106010190@njust.edu.cn, sunyh@seu.edu.cn, sun-quansen@njust.edu.cn, rzww@njust.edu.cn, xuxian@seu.edu.cn

This paper was produced by the IEEE Publication Technology Group. They are in Piscataway, NJ.

Manuscript received April 19, 2021; revised August 16, 2021.

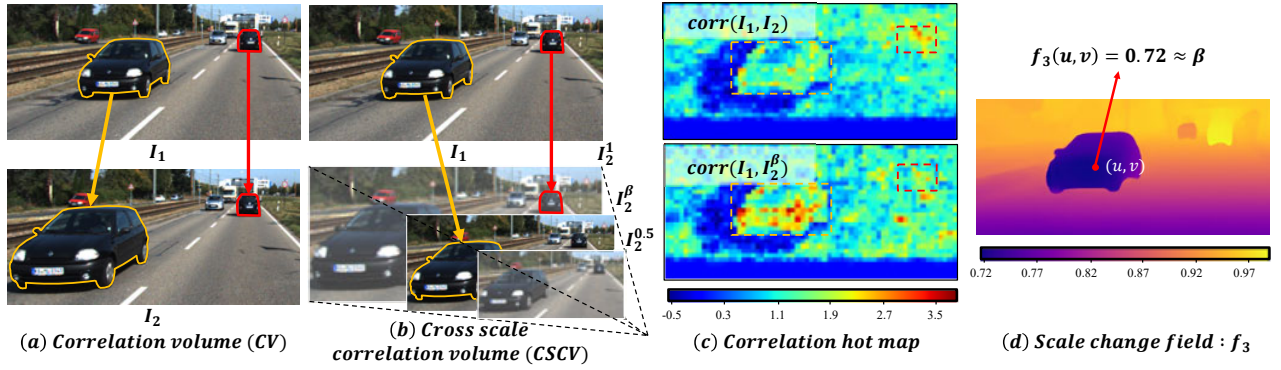


Fig. 2. Cross-scale matching idea. We match cars between two consecutive frames I_1 and I_2 , where the yellow car is close to the camera and the red car is relatively static to the camera. (a) The CV module in the optical flow baseline [20] matches cars at the same scale, while the yellow car cannot match well because of the scale change. (b) CSCV matches objects in the 3D scale space, so that each object can achieve the perfect matching of position and scale simultaneously. (c) We visualize the correlation hot map sampled from the CV module. $\text{corr}(I_1, I_2^\beta)$ means that CV is built based on I_1 and I_2 , where the meaning of each pixel point (x, y) is the correlation between the point $I_1(x, y)$ and its corresponding point $I_2^\beta(\beta(x + \mathbf{f}(x, y)), \beta(y + \mathbf{f}(x, y)))$, \mathbf{f} is the ground truth optical flow. **The correlation of the scale-changed yellow car in $\text{corr}(I_1, I_2)$ is smaller than that of the scale-invariant red car, while the correlation of the yellow car in $\text{corr}(I_1, I_2^\beta)$ is higher, which proves that the scale change has an important impact on the stability of optical flow matching.** (d) Dense scale change field f_3 estimated from our CSCV, the value of each pixel represents the scale change ratio.

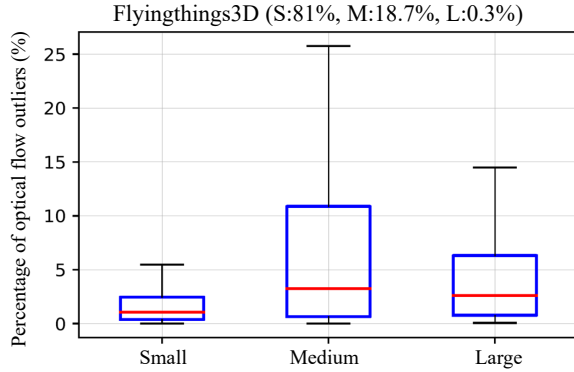


Fig. 3. Box plot of optical flow error distribution in different scale change regions. We measure the scale change of different regions based on scale change rate s_p , which means the size change percentage of objects between two frames. We pre-trained the optical flow network RAFT on Flyingthings3D and evaluated it on the test set. During the evaluation, s_p is divided into three intervals: (0, 2.5%), (2.5%, 32.5%), and (32.5%, $+\infty$), corresponding to small(S), medium(M), and large(L) scale change regions. The subgraph title provides the percentage of each region in the test dataset. Only non-occluded pixels have been included in the evaluation. Results indicate that the error of the optical flow baseline is concentrated in regions with significant scale changes, which is consistent with our motivational analysis and Lowe et al.’s judgment [25].

in 2005, Mikolajczyk [26] successfully estimated the scale changes of the clock tower captured at different focal lengths using similar scale selection techniques. Through the successful experience of predecessors, we recognize that features have good stability and separability in the scale dimension. **Therefore, we attempt to extend optical flow matching from a 2D pixel plane to a 3D scale space, match features at the correct position and scale, solve the impact of scale changes on optical flow matching, and provide more depth clues by estimating the scale change.**

Our Method. We propose an enhanced cross-scale normalized scene flow (NSF) search framework based on RAFT (ScaleRAFT). The core feature is to replace the original single scale correlation volume (CV) with cross-scale correlation

volume (CSCV), to achieve cross-scale feature matching by calculating the correlation between different position and scale feature pairs. As shown in Fig. 2, CSCV matches objects with different motion velocities (depth direction) at different scales, achieving more stable feature matching. The matching behavior in the scale dimension also directly provides the scaling factor of each object between two frames. Based on previous work [18], we can naturally obtain the corresponding depth change rate, which helps the network alleviate dependence on regression and depth values. We demonstrate in Fig. 1 that ScaleRAFT can robustly estimate 3D motion and extend it to downstream 3D tasks.

Expect scale changes, there are typical occlusion and over-fitting issues in three-dimensional flow. We have improved the commonly used truth supervision mode and proposed a training pipeline that combines self-supervision and truth. Specifically, we iteratively generate flight foreground with random textures and shapes to cover the original image pairs, and calculate the 3D flow truth of the flight foreground to replace the original position labels. Previous works often use solid coloured blocks to cover the source image to create occlusion actively. However, this behaviour encouraged the network to rely overly on regression to estimate optical flow, resulting in poor generalization. Our hybrid training pipeline actively creates occlusion while forcing the network to learn the 3D flow of randomly moving foreground through texture matching, ultimately balancing occlusion prediction and texture matching learning.

To broaden the application scope of our framework, we added a rigid background optimization module (RBO) after the basic ScaleRAFT in this paper. Based on depth values and semantic classification, RBO further optimized the background part of the 3D flow, upgrading the original normalized scene flow method to the RGBD-based scene flow method (called ScaleRAFT-RBO). Moreover, to further verify the rationality and universality of the cross-scale matching approach, we ported the core module CSCV to the advanced scene flow

method RAFT3D (called SacleRAFT3D) and directly replaced the original CV correlation volume with CSCV, changed the calculation method of deep motion from regression to scale matching. Compared with RAFT3D, ScaleRAFT3D changes the direct regression prediction mode, providing more reliable clues for depth motion prediction.

Significant performance improvement validates our motivation. On KITTI [27], ScaleRAFT far surpasses all NSF methods, reducing SF-all to 6.12%. As a monocular method, ScaleRAFT even outperforms the method using additional depth information (LiDAR, RGB-D) in foreground metrics, refreshing the optimal performance of foreground scene flow and foreground optical flow. ScaleRAFT3D also achieved significant performance improvement compared to baseline RAFT3D, with SF-all reduced from 5.77% to 4.74%, proving that our cross-scale matching technique has a certain degree of universality. In addition, although not specifically designed for RGBD, our ScaleRAFT-RBO still achieves leading performance with SF-all only at 4.20%. On Flyingthings3D [28], we followed the training and testing process of RAFT3D. The end-to-end 3D error of ScaleRAFT3D was reduced from 6.4cm to 4.9cm compared to the baseline model. Our method also has strong generalization and robustness. We demonstrated the excellent performance of ScaleRAFT in the field driving scenes without fine-tuning and daily scenes with non-rigid objects in the **Supplementary Material Sec. III**.

- We propose a simple yet powerful normalized scene flow framework, ScaleRAFT, which unifies optical flow and depth motion estimation into one model, achieving more robust 3D flow estimation.
- We propose a self-supervised truth mixing training pipeline that balances the learning of occlusion regression and texture matching.
- We built two different directions of extension ScaleRAFT-RBO and ScaleRAFT3D based on the basic framework ScaleRAFT, expanding the application scope of the ScaleRAFT framework and proving the universality of cross-scale matching ideas.
- We test our methods on various 3D flow tasks and generally achieve significant improvements over previous state-of-the-art methods.

Differences from The Preliminary Version. A preliminary version of this work, Scale-flow [29], has been accepted by ACM MM 2022. Compared to the preliminary version, our expanded paper has added several new contents: (i) We introduce a self-supervised and truth mixed training pipeline that helps the network better balance the learning between occlusion fitting and texture matching, alleviate potential overfitting problems during training, and better predict motion prospects. (ii) We have extended the original monocular method to an RGBD version by adding a background rigid optimization module, expanding the application scope of our method. (iii) We have extended the core module CSCV to other advanced RGBD scene flow methods, further verifying the effectiveness of cross-scale matching ideas. (iv) We also demonstrated more ablation studies, particularly analyzing the effectiveness of mixed training pipelines. (v) We validated the effectiveness of

our proposed method and two extensions on the official KITTI testing benchmark.¹ (vi) We further validated our method's scene flow performance on the Flyingthings3D dataset.

We have released a demo program² for 3D motion estimation in daily scenes and evaluation corresponding to the key results in the article. Welcome to check.

II. RELATED WORKS

In this section, we first introduce the optical flow task and scene flow task closely related to 3D flow, and then present the motion-in-depth estimation and cross-scale matching technique, which is the primary source of inspiration for the CSCV module.

A. Optical Flow

Early methods [30]–[33] viewed optical flow as an optimization problem for minimizing energy. Based on the regularization term and the constant brightness assumption, the optical flow results are optimized iteratively. Some recent excellent works have inherited their ideas [13], [20], [34], gradually updating the optical flow field through correlation matching and warping techniques. Compared with the previous methods [21], [35]–[43] of directly using convolutional networks to regress optical flow, the method based on correlation matching has a clearer theoretical background and more robust results. In this work, inspired by the successful experience of correlation matching, we extended this matching pattern to the scale dimension based on CSCV, improving the scale robustness of the optical flow baseline model.

It is worth mentioning that although some previous optical flow works [20], [44]–[49] also used the idea of scale, our method differs fundamentally from theirs. Previous works are often based on multi-scale technology to increase the network receptive field, improve the inference speed, and strengthen the loss function. However, it is still image-to-image matching in essence. CSCV introduces a pattern for optical flow matching in scale space, a brand-new attempt.

B. Scene Flow

Scene flow aims to estimate the motion of pixels in 3D space, which is the main component of the 3D flow problem.

Methods Based on Rigid Assumption. Early methods [50], [51] decompose the image into rigid blocks, and iteratively optimize the 3D motion of the rigid blocks based on the rigid assumption and regularization terms. In recent scene flow methods [13]–[15] based on convolutional networks, a semantic network is often introduced to judge whether pixels belong to the same rigid object, and the 3D flow is optimized again according to the semantic results. Although it performs well on datasets, such methods are difficult to promote and apply in field scenarios due to the need for depth information and additional semantic labels. In addition, sub-modules such as 3D flow and semantic estimation are independent. Any

¹https://www.cvlibs.net/datasets/kitti/eval_scene_flow.php

²<https://github.com/HanLingsjik/CSCV>

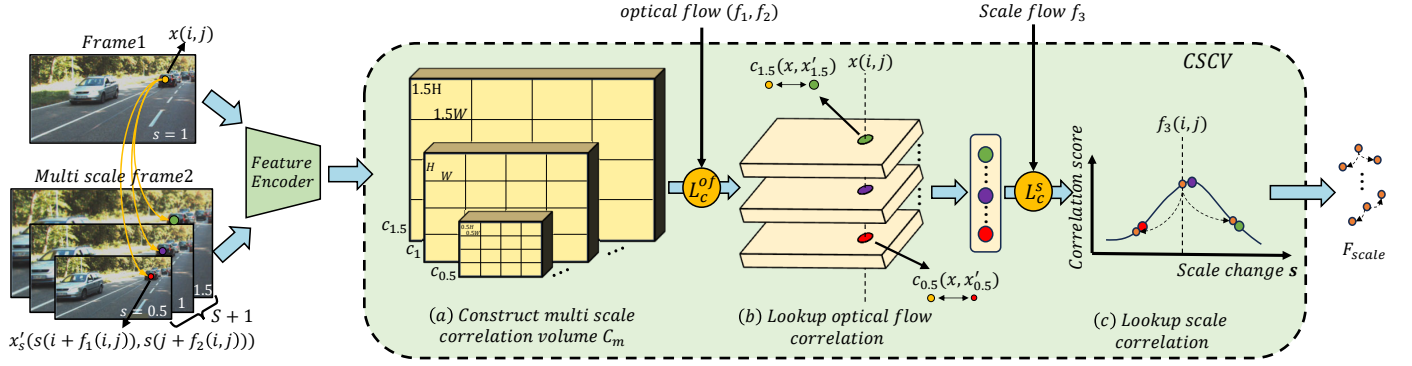


Fig. 4. The complete structure of cross-scale correlation volume (CSCV). The CSCV module is composed of three parts: multi scale correlation volume C_m , optical flow lookup operator L_c^{of} , and scale lookup operator L_c^s . After the optical flow field (f_1, f_2) and scale change field f_3 are input, the optical flow feature F_{of} and multi-scale optical flow feature F_{multi} are first sampled from C_m by the L_c^{of} operator, while the scale feature F_{scale} is obtained from F_{multi} by the L_c^s operator.

defects in sub-module will affect overall performance, as the entire pipeline depends on its results.

Methods Based on Point Cloud. Point cloud based methods [52]–[61] capture 3D point clouds of the surrounding environment through an active laser or stereo camera, and establish the corresponding relationship between two frame point clouds to estimate 3D motion. However, this kind of method is limited by the sparse results and limited range, which is challenging to apply in more common video scenes. There is also a point cloud method based on the fusion framework, Camliflow [14]. By highly fusing the point cloud and the optical flow pipeline, the two pipelines can obtain complementary results at the same time. Camliflow achieves end-to-end scene flow estimation, but it still has the problem of depth information dependence.

C. Motion-in-depth (MID)

MID describes the motion in the depth direction through the scale change of depth. It has many practical application scenarios, such as time-to-collision (TTC) estimation, LiDAR scene flow, scene flow, Etc. MID is also the core indicator of our ScaleRAFT.

Early TTC works [62]–[64] estimated the MID by tracking the motion trajectory of the interest points and building a motion model. Because the distribution of the interest points is random, this kind of method often makes it hard to pay attention to the primary target, yielding only sparse and low-precision results. Binary TTC [19] is a successful TTC scheme proposed recently, which can regress a dense MID field segmentally. Binary TTC sends the scaled image to the encoder to directly return the MID result of a certain range, and the specific range depends on the scaling factor. Therefore, a complete MID estimation requires multiple regressions to cover the complete MID interval. Unlike them, ScaleRAFT only needs one calculation to get complete and dense MID results.

Yang & Ramanan [18] proposed the only monocular normalized scene flow method. They obtained dense MID results based on optical flow step-wise regression optical expansion and MID. However, the same as previous TTC work, they

separated optical flow and MID estimation, resulting in the depth motion estimation result dependent on the optical flow result. Unlike them, ScaleRAFT integrates optical flow and depth motion estimation into a harmonious task based on CSCV, making information blend and help each other. In addition, the cross-scale matching mechanism can also help the optical flow module more accurately estimate the objects with scale changes.

D. Cross-scale Matching

Cross-scale matching aims to establish the correspondence between objects in different frames [65]–[75], and the scales of objects in these frames often have large changes, which is a difficult problem faced by current optical flow methods. In the early works, SIFT [25] obtains scale-invariant features in the scale space through hand-designed feature extraction operators, and then matches objects of different scales based on these stable features. In addition to being used for matching, cross-scale matching technology can also be used to estimate the scale changes of objects between frames. As early as 2005, Mikolajczyk [26] used Lindeberg’s scale selection method [76] to successfully estimate the optical expansion of clock towers captured at different focal lengths. Inspired by the above works, CSCV performs optical flow matching in scale space and estimates a dense scale change field based on the cross-scale matching results.

III. OUR APPROACH

Recurrent All-pairs Field Transforms (RAFT) [20] is the state-of-the-art optical flow baseline [77], which constructs a 4D correlation volume over the all-pairs pixel and iteratively optimizes the optical flow field through the GRU optimizer. In this section, we use a cross-scale matching module (CSCV) to reconstruct the RAFT baseline and propose the new monocular 3D flow method called ScaleRAFT. The 3D flow estimated by ScaleRAFT consists of a 2D optical flow field and a 1D motion-in-depth (MID) field, where the MID is obtained by converting the scale change field.

The framework structure of ScaleRAFT is shown in Fig. 5. CSCV replaces the original CV module in RAFT, and an

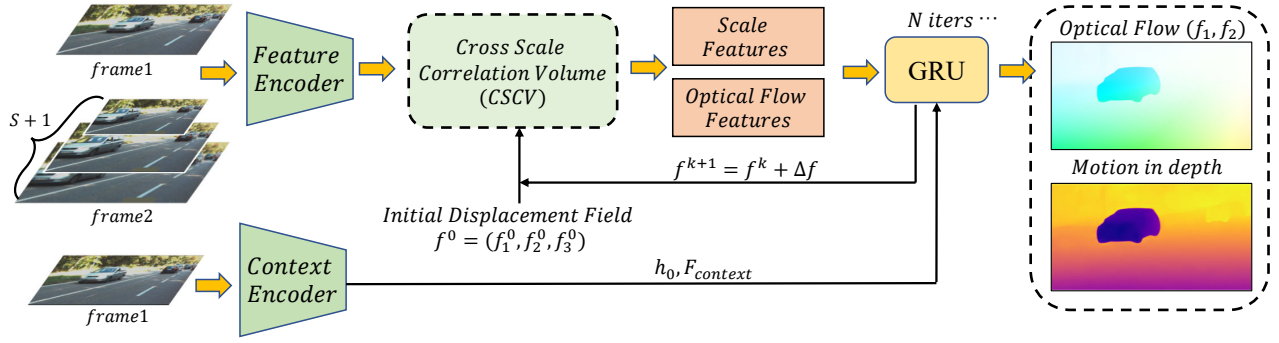


Fig. 5. Overview of ScaleRAFT. First, the frame2 is multi-scaled by bilinear interpolation, and fed to the feature extractor with the frame1 to obtain multi-scale features. Then a cross-scale correlation volume (CSCV) is established based on the multi-scale feature pairs, from which the correlation features about the current field can be sampled. Finally, the extracted correlation features are sent to the GRU optimizer to iteratively optimize an optical flow field and a scale change field. The MID result can be converted according to the scale change field by Eq.19.

additional optical expansion output head is added after the GPU module to predict the scale change field f_3 required for CSCV sampling. Combining with previous work [18], we convert the scale change field f_3 into motion-in-depth (MID), so that ScaleRAFT can be widely used in various monocular 3D flow tasks.

It is worth mentioning that ScaleRAFT is an end-to-end monocular 3D flow method. It integrates optical flow and depth motion prediction into a unified and harmonious matching framework through CSCV. We demonstrate in experiments that ScaleRAFT has impressive performance improvements and better robustness compared to previous monocular 3D flow methods. In the following parts, we will introduce in sequence: The construction and training process of ScaleRAFT (III-A, III-B, III-C, III-D); How to convert the results of network estimation into a 3D motion field (III-E); RGB-D extension based on rigid background optimization (III-F); Extend CSCV to other RGBD methods (III-G).

A. Feature Extraction

Feature Encoder. We use a convolutional network g_θ with 6 residual connections to extract features. As the number of layers increases, the feature channel gradually becomes wider, and the image size gradually becomes smaller, where $g_\theta : \mathbb{R}^{H \times W \times 3} \rightarrow \mathbb{R}^{(H/8) \times (W/8) \times D}$ ($D = 256$).

Context Encoder. Following RAFT, we build a context encoder h_θ ($D = 384$) with the same structure as g_θ . This context encoder extracts context features $F_{context}$ ($D = 192$) and implicit features h_0 ($D = 192$) from I_1 , where the implicit features are used to initialize the internal parameters of GRU optimizer.

B. Cross-scale Correlation Volume (CSCV)

In this part, we introduce the construction of the cross-scale correlation volume (CSCV) module. As shown in Fig. 4, firstly, the correlation volume C_m is constructed from the dot multiplication of input multi-scale features. Then the multi-scale optical flow correlation features F_{multi} and scale correlation features F_{scale} are extracted from C_m successively using the optical flow lookup operator L_c^{of} and scale lookup operator L_c^s .

The Input of CSCV. The main function of CSCV is to sample the correlation features of the current input 3D flow field. Specifically, the input 3D flow field is composed of an optical flow field (f_1, f_2) and a scale change field f_3 . The optical flow field describes the displacement of pixels between two frames, and the scale change field is the reciprocal of optical expansion (OE), which describes the pixel scaling factor of the second frame for perfect matching the first frame.

When constructing C_m , multi-scale image features are extracted by a residual convolutional network g_θ , where the input of the network is I_1 and P_{I_2} :

$$P_{I_2} = \{I_2^s \mid s = 0.5, 0.5 + 1/S, \dots, 1, \dots, 1.5\} \quad (1)$$

where $I_2^s \in \mathbb{R}^{(H \times s) \times (W \times s) \times 3}$, S specifies the degree of refinement of the input scale, which is generally set to 4 in our experiment.

Multi Scale Correlation Volume. The multi scale correlation volume C_m is a collection of multiple 4D correlation matrices. The construction of the 4D matrix follows RAFT [20], which can be sampled by the coordinates of a pair of matching points. The sample result is the correlation of these two points. Specifically, for the given image features $g_\theta(I_2^s) \in \mathbb{R}^{(H \times s) \times (W \times s) \times D}$ and $g_\theta(I_1) \in \mathbb{R}^{H \times W \times D}$, dot them to obtain a single 4D correlation matrix c_s :

$$c_s(g_\theta(I_2^s), g_\theta(I_1)) \in \mathbb{R}^{H \times W \times (H \times s) \times (W \times s)} \quad (2)$$

$$(c_s)_{ijkl} = \sum_h g_\theta(I_2^s)_{ijh} \cdot g_\theta(I_1)_{klh}$$

where (i, j) , (k, l) are the coordinates of two pairs of points on I_2^s and I_1 respectively, h is the dimension index of the feature, and c_s is the 4D correlation volume between I_1 and I_2 with scale s .

The final C_m is a set about c_s :

$$C_m = \{c_s \mid s = 0.5, 0.5 + 1/S, \dots, 1, \dots, 1.5\} \quad (3)$$

Optical Flow Lookup Operator. We define the optical flow lookup operator L_c^{of} to sample the correlation features corresponding to the current optical flow field (f_1, f_2) from C_m .

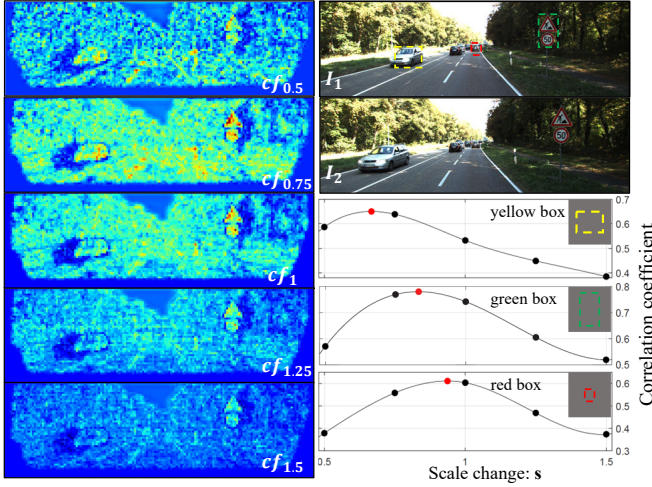


Fig. 6. Visualization of the scale matching by CSCV. On the left is the multi-scale optical flow feature F_{multi} when $S = 4$ and $r_f = 0$. The redder the color of the point, the higher the correlation. On the right is the correlation curve, where the value of each black point is the mean value of the points in the box on the left, and the red point is the extreme value obtained by interpolation. The extreme points of the cars in the yellow box and the signs in the green box tend to be 0.5 and 0.75, which means they are moving toward the camera rapidly. The extreme point of the red box tends to 1, which means that the object is relatively stationary with the camera.

Given an optical flow field (f_1, f_2) , it maps each pixel $x = (k, l)$ in I_1 to $x' = s(k + f_1(k, l), l + f_2(k, l)) = (i, j)$ in I_2^s , L_c^o samples in the neighborhood $N_{x'}^f$ of x' :

$$N_{x'}^f = \{ (i + d_u, j + d_v) \mid d_u, d_v \in \{-r_f, \dots, r_f\} \} \quad (4)$$

where r_f is an integer, it specifies the size of the sampled neighborhood, and neighborhood sampling provides the optimal direction for the network.

Based on the sampling coordinates provided by $N_{x'}^f$, we conducted bilinear interpolation sampling for each c_s in C_m to get the collection of multi-scale optical flow correlation feature F_{of} :

$$F_{of} = \{cf_s \mid s = 0.5, 0.5 + 1/S, \dots, 1, \dots, 1.5\} \quad (5)$$

where $cf_s \in \mathbb{R}^{H \times W \times (2r_f+1) \times (2r_f+1)}$.

Finally, we spliced all the elements in F_{of} to form a 5D correlation matrix $F_{multi} \in \mathbb{R}^{H \times W \times (2r_f+1) \times (2r_f+1) \times (S+1)}$. The newly added fifth dimension is the scale dimension, which can be used to sample the correlation between the I_2 features of different scales and the I_1 features of the original scale.

Scale Lookup Operator. We define the scale lookup operator L_c^s to sample the correlation features corresponding to the current scale change field f_3 from F_{multi} .

Given a scale change field f_3 , it describes the scale change of a pixel block between two frames. The scale change field f_3 maps each pixel $x = (k, l)$ in I_1 to $x' = f_3(k, l) \times (k + f_1(k, l), l + f_2(k, l)) = (i, j)$ in $I_2^{f_3(k, l)}$, L_c^s sample the neighborhood $N_{x'}^s$ in the scale direction of point x' :

$$N_{x'}^s = \{ f_3(k, l) + d_s \mid d_s \in \{-r_s, \dots, r_s\} \} \quad (6)$$

where r_s is a real number, we set $r_s = 1/S$ in our experiments, $N_{x'}^s$ provides optimal awareness in the scale direction.

Based on the sampling coordinates provided by $N_{x'}^s$, we sample in F_{multi} based on bilinear interpolation, and splice the results into scale correlation feature $F_{scale} \in \mathbb{R}^{H \times W \times (2r_f+1) \times (2r_f+1) \times (2r_s+1)}$.

We follow the RAFT strategy to extract the optical flow correlation feature $F_{of} \in \mathbb{R}^{H \times W \times (2r_f+1) \times (2r_f+1) \times 4}$, which is sampled from c_1 (2×2 pooling for three times) by L_c^{of} .

C. Updating Displacement Field

Initialization. We initialize the optical flow field (f_1^0, f_2^0) to 0 everywhere and scale change field f_3^0 to 1 everywhere, initial h_0 is given by context encoder.

Updating. We use the residual update to estimate the displacement field $f^{k+1} = f^k + \Delta f$, which is based on the gating activation unit GRU, and replace the full connection layer with the convolution layer:

$$\begin{aligned} z_t &= \text{Sigmoid}(\text{Conv}(W_z \cdot [h_{t-1}, x_t])) \\ r_t &= \text{Sigmoid}(\text{Conv}(W_r \cdot [h_{t-1}, x_t])) \\ \tilde{h}_t &= \tanh(\text{Conv}(W \cdot [r_t * h_{t-1}, x_t])) \\ h_t &= (1 - z_t) * h_{t-1} + z_t * \tilde{h}_t \end{aligned} \quad (7)$$

Eq (7) shows the process of the GRU optimizer iteratively updating the hidden parameter h_t , where the input is h_{t-1} and x_t , the output is the updated h_t , and W_z, W_r, W is the parameter to be learned. x_t is the combination of displacement field $f = (f_1, f_2, f_3)$, correlation feature F_{of} and F_{scale} , and context feature $F_{context}$.

The residual $\Delta f = (\Delta f_1, \Delta f_2, \Delta f_3)$ for updating is estimated from h_t by a simple two-level convolution module:

$$\begin{aligned} (\Delta f_1, \Delta f_2) &= \text{Conv}(\text{ReLU}(\text{Conv}(h_t))) \\ \Delta f_3 &= \tanh(\text{Conv}(\text{ReLU}(\text{Conv}(h_t)))) \end{aligned} \quad (8)$$

Considering that the scale field requires more detailed estimation, we replaced the GRU with a small Unet [78] network and performed an additional update of f_3 .

Upsampling. The network prediction output is 1/8 resolution. The results used for prediction and training need upsampling. Here we follow the previous work [20], linearly weight upsampling based on the 3×3 neighborhood of coarse-resolution pixels.

D. Hybrid Training Pipeline

We use a combination of self-supervised and ground truth methods to train our model. In this section, we focus on introducing the self-supervised data generation pipeline. As shown in Fig. 7, details are as follows.

Creating Random Flight Foregrounds. Firstly, based on the randomly generated closed curve (generated by the Bessel curve), crop the corresponding image block p on a random image, and then project it to the P in the camera coordinate system:

$$p(i) = (x, y, 1) \quad (9)$$

$$P(i) = ZK^{-1}p(i) = (X, Y, Z) \quad (10)$$

where i is the point contained in p , K is the camera intrinsic matrix, and the depth Z of all pixels in P is 1.

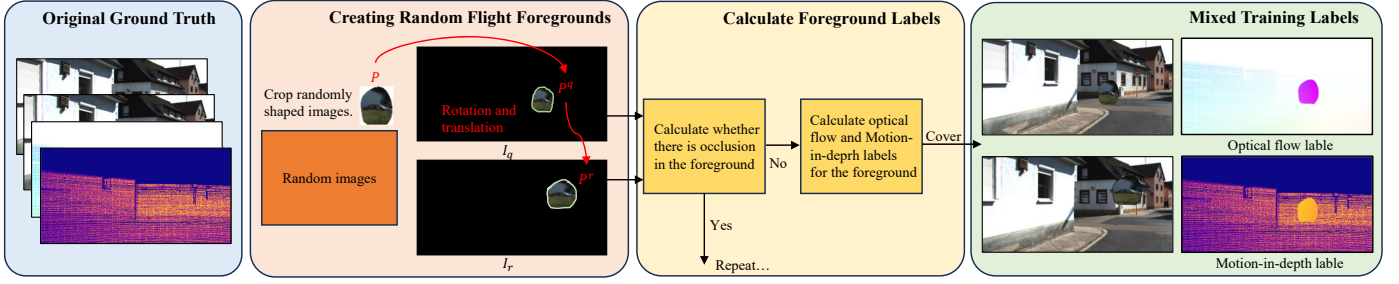


Fig. 7. Hybrid training data generation pipeline. Our pipeline is divided into three parts. Firstly, we crop randomly shaped foreground image blocks from random images and perform spatial rotation and translation transformations between two frames. Afterwards, it is determined whether the image block has been occluded (flying out of the image range). If no occlusion has occurred, the corresponding optical flow truth value and depth change truth value are calculated. Finally, iteratively add the generated flight foreground to the original image and update the related truth labels at the same time.

After obtaining P , we first perform the initial spatial transformation to obtain P^q , and then project it onto the pixel coordinate system to get the p^q on image I_q :

$$P^q(i) = R_r P(i) + T_r \quad (11)$$

$$p_q(i) = K P^q(i) \quad (12)$$

among them, R_r and T_r are the rotation matrix and translation matrix of random values. Similarly, we perform the spatial transformation on P^q to obtain P^r and project it onto the pixel plane to get p^r on image I_r .

Note that the captured image blocks here lean towards random textures, as we found that using foreground flying objects with clear semantic information (such as complete car, human, and animal contours) does not perform as well as random textures. Specifically, when occlusion occurs, the network becomes overly confident in inferring the motion of the occluded part of the object as planar motion. Random textures can encourage networks to calculate the motion of these flying foreground based on texture matching, and balance the learning weight with occlusion regression.

Calculate Foreground Labels. Before calculating the label for the flight foreground, it is necessary first to determine whether there is an occlusion in the foreground. Because the flight foreground is primarily a random texture, the network cannot make reasonable inferences about the occluded parts. We propose a difference rate Df indicator to measure whether the prospect is retained:

$$Df = \frac{|N_r - N_q|}{|N_r + N_q|} \quad (13)$$

where N_q and N_r represent the number of foreground flying object pixels in the first and second frames, respectively. In the experiment, we only used flight prospects with Df less than 0.3 to ensure no significant obstructions or great scale changes during the flight.

After filtering, calculate the accurate value of the flight foreground optical flow and the true value of the depth change rate as follows:

$$f_{fg} = p_r - p_q \quad (14)$$

$$\tau_{fg} = Z^r / Z^q \quad (15)$$

where f_{fg} is the optical flow of the flight foreground, and τ_{fg} is the corresponding motion-in-depth.

Optical Flow Loss. We supervise the optical flow results with L_1 distance between prediction and ground truth, the optical loss \mathcal{L}_f is defined as:

$$\mathcal{L}_f = \sum_{k=1}^N \gamma^{N-k} (\|f_1^k - f_{1gt}\|_1 + \|f_2^k - f_{2gt}\|_1) \quad (16)$$

we set $\gamma = 0.8$, $N = 12$ in our experiments, the $f_{gt} = (f_{1gt}, f_{2gt})$ is composed of a hybrid of truth labels from the dataset and the generated f_{fg} labels.

Scale Change Field Loss. According to Eq (19), the Scale change field f_3 equal to MID τ under the slight rotation assumption, which allows us to use the scene flow datasets to train the f_3 . The loss is defined as follows:

$$\mathcal{L}_s = \sum_{k=1}^M \gamma^{M-k} \|f_3^k - \tau_{gt}\|_1 \quad (17)$$

where τ_{gt} is also a hybrid of true values τ and generated labels τ_{fg} , $\tau = Z'_{gt}/Z_{gt}$, Z'_{gt} and Z_{gt} are the ground truth depths of matching pixels in the second frame and the first frame, we set $\gamma = 0.8$, $N = 13$ in our experiments.

The overall loss function is:

$$\mathcal{L} = \mathcal{L}_f + \mathcal{L}_s \quad (18)$$

E. Convert ScaleRAFT output to 3D motion

Referring to previous work [18], we converted the 3D motion (f_1, f_2, f_3) into motion-in-depth and scene flow. Firstly, based on Yang's [18] derivation, we can obtain the following approximate equation:

$$f_3 \approx \frac{Z'}{Z} = \tau \quad (19)$$

where, Z and Z' is the depth of the object in two frames, and τ is the motion-in-depth.

Furthermore, based on Eq.19, we can derive the relationship between (f_1, f_2, f_3) and scene flow t :

$$t = ZK^{-1}[(f_3 - 1)Cd + f_3(f_1, f_2)] = Z\bar{t} \quad (20)$$

where Cd is the image coordinate index matrix, normalize scene flow $\bar{t} = K^{-1}[(f_3(p) - 1)p + f_3(p)f]$. We have presented a detailed derivation process in the **Supplementary Material. I**.

F. Expand ScaleRAFT to RGB-D Method

In this section, we used a simple yet practical rigid background optimization (RBO) approach to upgrade ScaleRAFT to the RGBD version.

Specifically, we first remove manually specified motion foreground objects (cars and pedestrians in KITTI) from the current frame based on semantic masks [79] to obtain the background point set p_{2d}^1 . Then, based on depth values Z and optical flow $\mathbf{f} = (f_1, f_2)$, we calculate the 3D coordinates P_{3d}^1 of pixels in the first frame and their corresponding planar coordinates p_{2d}^2 in the second frame:

$$P_{3d}^1 = ZK^{-1}p_{2d}^1 \quad (21)$$

$$p_{2d}^2 = p_{2d}^1 + \mathbf{f}(p_{2d}^1) \quad (22)$$

At this point, the rigid background optimization problem is transformed into a PnP problem. We use the *solvePnP* function in OpenCV [80], [81] to solve the corresponding rotation and translation between two frames:

$$R_{bg}, T_{bg} = \text{solvePnP}(P_{3d}^1, p_{2d}^2, K) \quad (23)$$

Based on R_{bg} and T_{bg} , we consider the background pixels as a whole and recalculate the 3D motion t_{bg} of the background:

$$P_{3d}^2 = R_{bg}P_{3d}^1 + T_{bg} \quad (24)$$

$$t_{bg} = P_{3d}^2 - P_{3d}^1 \quad (25)$$

where t_{bg} is the optimized background scene flow, and we directly replace the original background result with it. The RBO idea has been indirectly or directly used in most current scene flow methods. Our RBO algorithm refers to the background optimization section in [14]. More details about RBO can be found in [13]–[15].

Why RBO? The main advantage of the cross-scale matching algorithm ScaleRAFT is that it can better estimate the moving foreground, while the most significant advantage of rigid optimization technology is that it can optimize the entire static background as a rigid object at once. These two algorithms are complementary in terms of characteristics. The outstanding performance demonstrated by ScaleRAFT-RBO in Tab. II demonstrates the effectiveness of this complementary combination.

G. Apply CSCV to RAFT3D

RAFT3D [13] is a state-of-the-art method for scene flow. It regresses scene flows directly from RGBD inputs based on RAFT baselines and iteratively optimizes the regression results through a rigid optimization layer. We extend CSCV to RAFT3D baseline (called ScaleRAFT3D) to further validate the effectiveness of cross-scale matching idea.

The overall structure of ScaleRAFT3D is similar to ScaleRAFT, both of which use CSCV to extract cross-scale matching features and iteratively optimize the 3D motion. The main difference is that ScaleRAFT3D adds a rigid optimization layer after the GRU optimizer and directly estimates the $SE(3)$ transformation field \mathbf{T} . In addition, in order to extract semantic information for rigid optimization, the original 6-layer convolutional context extractor has been replaced with

Resnet50 [82]. We have presented a detailed ScaleRAFT3D structure in the **Supplementary Material Sec. II**.

IV. EXPERIMENTS

We train and evaluate our method on the standard scene flow datasets including KITTI, Driving, Flyingthings3D, and MPI-Sintel. In section IV-A, we will detail our benchmark datasets and training settings. In section IV-B, we evaluate the performance of ScaleRAFT on the MID task, which is also the core indicator of monocular 3D flow. In section IV-C, we evaluate ScaleRAFT on the TTC task. In section IV-D, we submit the proposed methods to the KITTI's scene flow benchmark³ for comparison with the state-of-the-art scene flow methods. In section IV-E, we tested the performance of ScaleRAFT and ScaleRAFT3D on the Flyingthings3D. Finally, in section IV-F, we conduct ablation experiments.

A. Datasets and Training Setting

Dataset. The training and testing of ScaleRAFT require the use of scene flow datasets, so we selected the currently commonly used KITTI [27] and Flyingthings3D [28] for Evaluating, and training based on Driving [28], Sintel [83], KITTI and Flyingthings3D. Because KITTI provides an official test ranking platform and contains the most advanced results, we mainly conduct evaluations on KITTI.

Training Setup. For the KITTI evaluation, we first conduct unified pre-training on the virtual datasets (Driving, Sintel, Flyingthings3D) and then fine-tune separately according to different evaluation items. Specifically, for the MID task, we use the same strategy as Yang [18] to split the dataset, selecting one out of every five images in KITTI for evaluation (K-40) and the remaining 160 images for fine-tuning training (K-160). For the scene flow task, we use all 200 images (K-200) for training and submit the results to the official evaluation platform for evaluation. During pre-training, the image size is 368x768, batch = 6, iteration = 200K, lr = 0.0005, and the number of motion foreground is 1. When fine-tuning, the image size is 960x320, batch = 6, lr = 0.000125, iterations = 80K, and the number of motion foreground is 1.

For the Flyingthings3D evaluation, we followed the training and evaluation process of RAFT3D [13], trained 200K generations on the training set (lr = 0.00025), and evaluated our method on the testing set. Only pixels with a depth of less than 35m and not occluded were included in the evaluation.

B. Motion-in-depth (MID)

MID is the core indicator of monocular 3D flow methods. In order to prove the superiority of ScaleRAFT in estimating MID tasks, we compared ScaleRAFT with the stereo-based traditional scene flow methods, state-of-art MID methods and scene flow methods on K-40. We use the same criteria as predecessors [18] to define the loss:

$$Mid_{error} = ||\log(f_3) - \log(\tau_{gt})||_1 \cdot 10^4 \quad (26)$$

where τ_{gt} is the ground truth of MID.

³http://www.cvlibs.net/datasets/kitti/eval_scene_flow.php

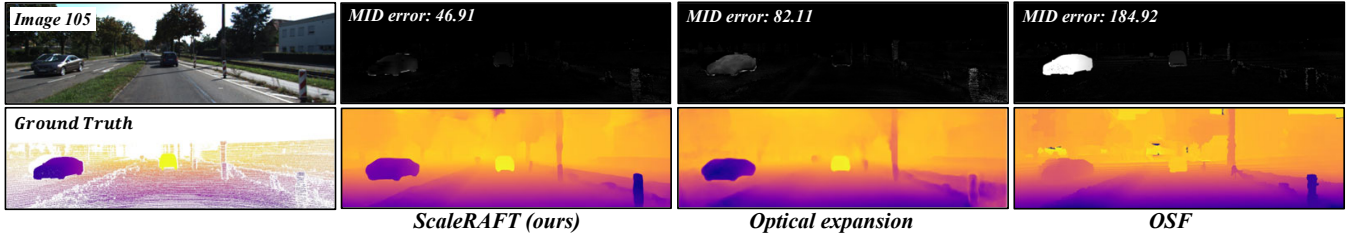


Fig. 8. Motion-in-depth results for images “105” in the K-40 set. For each of them, Up: input images and the error map, where the whiter the pixels, the greater the error. Down: ground truth and visualization of motion-in-depth. Our method is much more accurate than other methods.

TABLE I

MOTION-IN-DEPTH ESTIMATION ON K40. THE BEST AMONG ALL ARE BOLDED, AND THE SECOND BEST ARE UNDERLINED. OUR METHOD OUTPERFORMS THE MONOCULAR BASELINES BY A LARGE MARGIN.

Method	Input	Training set	$Mid_{error}(\downarrow)$	Time/s
OSF [50]	Stereo	K-160	115	3000
PRSM [51]	Stereo	K-160	124	300
Hur & Roth [84]	Mono	K-160	115.13	0.1
Binary TTC [19]	Mono	K-160	73.55	2.2
Optical expansion [18]	Mono	K-160	75	0.2
Scale-flow [29]	Mono	K-160	<u>48.9</u>	0.2
ScaleRAFT (ours)	Mono	K-160	42.08	0.2
RigidMask+ISF [15]	RGB-D	K-200	49.7	3.3
RAFT3D [13]	RGB-D	K-200	22.01	2
ScaleRAFT (ours)	Mono	K-200	<u>29</u>	0.2

We first compare with the stereo-based traditional approach: OSF and PRSM decompose the pixels into rigid blocks, and iteratively update the optical flow and depth field based on rigidity assumptions and hand-designed regularization terms. To get the MID result, we divide the depth of the second frame by the depth of the first frame. The experimental results show that our error is much smaller (115 v.s. 42.08) and in less time.

Then we compare with the state-of-the-art MID methods Optical expansion and Binary TTC. As shown in Fig. 8 and Tab. I, ScaleRAFT still has apparent advantages (73.5 v.s. 42.08). Unlike their direct regression of MID from optical flow, we embed the calculation of MID into optical flow matching. Convergence of information and end-to-end architecture make the final result more robust and accurate.

Finally, we compare ScaleRAFT with the state-of-the-art scene flow method. RigidMask and RAFT3D jointly optimize the calculated depth and optical flow field based on the rigidity assumption, and need to introduce additional semantic networks to calculate the rigidity mask. Because they used depth and optical flow networks pre-trained on KITTI, the training set is K-200. As shown in Tab. I, although they used additional input information, our method still has competitive accuracy (29 v.s. 22.01) and in less time, which reflects the effectiveness of our cross-scale matching strategy.

C. Time-to-collision (TTC)

Time-to-collision estimation is a crucial technique in path planning for autonomous robots [6]–[8], [87], which describes the collision time between moving objects and the observer

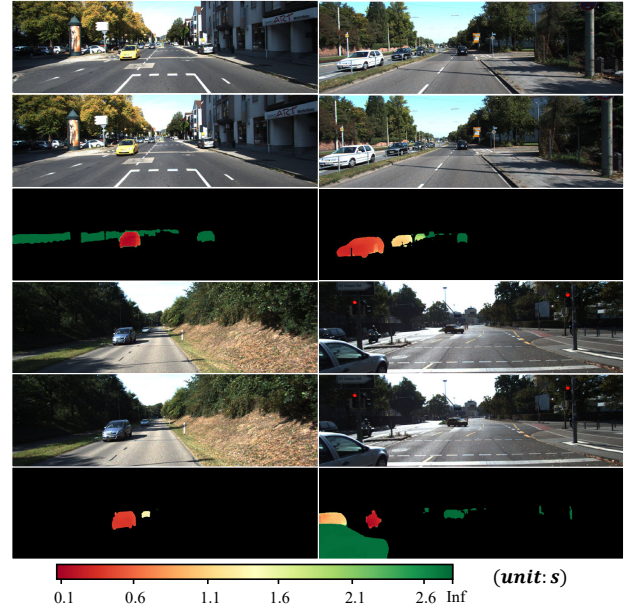


Fig. 9. Visualization of foreground target collision time. We visualized some of the TTC results in K-40; from top to bottom are two consecutive frames and the visualized collision time. The foreground mask is provided by the real-time segmentation algorithm Mseg [85].

plane. TTC can be estimated indirectly by MID:

$$TTC = \frac{Z}{Z - Z'}T = \frac{T}{1 - \frac{Z'}{Z}} = \frac{T}{1 - \tau} \quad (27)$$

where T is the sampling interval between two consecutive frames, for KITTI $T = 0.1s$, Z and Z' are the object's depth in frame1 and frame2, τ is the motion-in-depth.

TABLE III
PERCENTAGE ERRORS OF TIME-TO-COLLISION ESTIMATION ON K-40 VALIDATION SET

Method	Err-1s	Err-2s	Err-5s	Time/s
Binary TTC (Binary mode) [19]	2.4	3.16	3.25	0.0192
Optical expansion [18]	1.86	1.87	2.45	0.2
OSF [50]	<u>1.79</u>	2.93	4.03	3000
ScaleRAFT (ours)	0.87	1.23	1.31	0.2

Referring to Binary TTC, we regard TTC as a binary classification task, judging whether the TTC of each pixel in the image is less than $\{1s, 2s, 5s\}$. We evaluate the percentage of outlier pixel values in prediction results and only consider pixels close to the observation plane.

TABLE II

STATE-OF-THE-ART PUBLISHED METHODS ON KITTI SCENE FLOW BENCHMARK. RGB-D MEANS DEPTH AND MONOCULAR INFORMATION, AND MONO MEANS MONOCULAR INFORMATION. D1, D2, FL, AND SF IS THE PERCENTAGE OF DISPARITY, OPTICAL FLOW AND SCENE FLOW OUTLIERS. *-bg*, *-fg* AND *-all* REPRESENT THE PERCENTAGE OF OUTLIERS AVERAGED ONLY OVER BACKGROUND REGIONS, FOREGROUND REGIONS AND OVERALL GROUND TRUTH PIXELS. THE BEST AMONG ALL ARE BOLDDED, AND THE SECOND BEST ARE UNDERLINED. OUR MONOCULAR METHOD PERFORMS QUITE WELL, NOT ONLY FAR AHEAD OF SIMILAR MONOCULAR METHODS, BUT ALSO OUTPERFORMING RGBD-BASED METHODS IN FOREGROUND SCENE FLOW ESTIMATION, WHICH PROVES THAT THE CROSS-SCALE MATCHING CAN ACCURATELY ESTIMATE THE 3D MOTION.

Method	Typev	D1-bg	D1-fg	D1-all	D2-bg	D2-fg	D2-all	Fl-bg	Fl-fg	Fl-all	SF-bg	SF-fg	SF-all
CamLiFlow [14]	RGB-D	1.48	3.46	1.81	-	-	3.19	-	-	4.05	-	-	5.62
CamLiFlow-RBO [14]	RGB-D	1.48	3.46	1.81	1.92	8.14	<u>2.95</u>	<u>2.31</u>	<u>7.04</u>	<u>3.1</u>	<u>2.87</u>	<u>12.23</u>	<u>4.43</u>
RigidMask+ISF [15]	RGB-D	1.53	3.65	1.89	2.09	8.92	3.23	2.63	7.85	3.5	3.25	13.08	4.89
RAFT3D [13]	RGB-D	1.48	3.46	1.81	2.51	9.46	3.67	3.39	8.79	4.29	4.27	13.27	5.77
ScaleRAFT3D (ours)	RGB-D	1.48	3.46	1.81	1.93	8.16	2.97	2.37	9.26	3.51	2.91	13.87	4.74
ScaleRAFT-RBO (ours)	RGB-D	1.48	3.46	1.81	<u>1.93</u>	7.72	2.89	2.27	5.63	2.83	2.86	10.91	4.20
Optical expansion [18]	Mono	1.48	3.46	1.81	3.39	8.54	4.25	5.83	8.66	6.3	7.06	13.44	8.12
Binary TTC [19]	Mono	1.48	3.46	1.81	3.84	9.39	4.76	5.84	8.67	6.31	7.45	13.74	8.5
RAFT [20]	Mono	-	-	-	-	-	-	4.74	6.87	5.10	-	-	-
TPCV [86]	Mono	1.48	3.46	1.81	2.29	<u>7.63</u>	3.18	4.53	5.52	4.69	5.34	10.6	6.21
Scale-flow [29]	Mono	1.48	3.46	1.81	2.55	8.24	3.50	5.24	<u>5.71</u>	5.32	6.06	<u>11.32</u>	6.94
ScaleRAFT (ours)	Mono	1.48	3.46	1.81	<u>2.31</u>	7.42	3.16	4.45	4.76	4.50	5.31	10.18	6.12

Tab. III shows that ScaleRAFT achieves the lowest error in all time intervals, which proves our ScaleRAFT can estimate future collisions more accurately. As shown in Fig. 9, our method can effectively predict future collisions.

D. Scene Flow

Correctly estimating the 3D motion of an object is crucial for the robot path planning and action prediction task in a dynamic environment [4], [50]. Scene flow consists of optical flow and depth changes of matched pixels between two frames. In order to unify the evaluation standards with the most advanced methods, we use GA-Net [88] to obtain the depth of the first frame $D1$ and calculate the depth change through MID τ , where $D2 = \tau * D1$. The model was trained on the K-200 and tested on the KITTI public scene flow evaluation website.

ScaleRAFT. We first compare ScaleRAFT with monocular methods, as shown in Tab. II, ScaleRAFT leads in all monocular methods with significant advantages, consistent with the previous superior performance in motion-in-depth tasks. It proves the effectiveness of our ScaleRAFT framework in the field of monocular 3D motion estimation. We also compare ScaleRAFT with the state-of-the-art RGBD-based methods RAFT3D, CamLiFlow, and RigidMask+ISF. As shown in Tab. II, RGBD-based methods tend to get smaller Fl-bg errors, which is thanks to the aid of depth-based rigid assumption to optimize the background optical flow. Nonetheless, our monocular approach still achieves the best results on SF-fg. Moreover, our method showed a significant improvement in optical flow prediction performance compared to the baseline model RAFT.

ScaleRAFT-RBO Although ScaleRAFT is not a framework specifically designed for RGBD, ScaleRAFT-RBO still has particular advantages over other state-of-the-art methods. As shown in Tab. II, the performance of ScaleRAFT-RBO exceeds most existing methods (4.43 v.s. 4.20). This excellent performance is mainly due to RBO compensating for the weakness

of monocular methods in background estimation and CSCV alleviating the difficulty of foreground object matching.

ScaleRAFT3D. Compared with the baseline RAFT3D, ScaleRAFT3D has great advantages in all major indicators, especially the overall scene flow error SF-all has been dropped from 5.77 to 4.74, and has competitive accuracy in RGBD-based methods. We have noticed that the foreground part of ScaleRAFT3D has not improved. This is because RAFT3D is a system composed of multiple sub-modules, and the final result depends on the semantic-based rigid optimization pipeline. Strengthening a single 3D flow pipeline cannot comprehensively improve the performance of the baseline model.

E. Flyingthings3D

To further verify the performance of our method, we have carried out more tests on the larger virtual dataset Flyingthings3D (Fly3D). We followed the configuration of RAFT3D [13] for training and evaluation. Specifically, trained 200k generations on the training set and evaluated our network with 2D and 3D endpoint errors (EPE). The 2D EPE is defined as the Euclidean distance between the real and predicted optical flow. 3D EPE is the European distance between the real and predicted scene flow.

In the testing phase, we used the split strategy proposed in FlowNet3D [53], containing 2007 test examples sampled from the Fly3D's test set (Fly3D-2007). Only non-occluded pixels with depth $< 35m$ were included in the evaluation.

We first compared our ScaleRAFT3D with the baseline model RAFT3D. As shown in Tab. IV our expanded method has a leading advantage in all indicators, which proves that our scale matching strategy is superior to the regression strategy in RAFT3D.

We also explored the performance of our monocular method ScaleRAFT on the Fly3D. As shown in Tab. IV, ScaleRAFT has a leading performance in 2D indicators compared with RAFT, and has a certain competitiveness in 3D indicators compared with LiDAR and RGB-D methods, which proves that the ScaleRAFT framework can adapt to data containing challenging scenarios.

TABLE IV

PERFORMANCE COMPARISON ON THE FLYINGTHINGS3D TEST SET. WE FOLLOWED THE SETUP OF FLOWNET3D IN WHICH ONLY NON-OCCLUDED POINTS WITH DEPTHS LESS THAN 35M ARE CONSIDERED FOR EVALUATION. $\delta_{2D} < 1px$ MEANS THE PERCENTAGE OF OPTICAL FLOW ENDPOINT ERROR LESS THAN 1 PIXEL, $\delta_{3D} < 0.05m$ MEANS THE PERCENTAGE OF PIXELS WITH ENDPOINT ERROR LESS THAN 0.05M.

Method	Input	2D Metrics		3D Metrics		
		$\delta_{2D} < 1px(\uparrow)$	$EPE(\downarrow)$	$\delta_{3D} < 0.05m(\uparrow)$	$\delta_{3D} < 0.10m(\uparrow)$	$EPE(\downarrow)$
RAFT [20]	Mono	77.2%	3.76	—	—	—
ScaleRAFT (ours)	Mono	80.5%	3.41	31.7%	51.2%	0.206
FlowNet3D [53]	LiDAR	—	—	25.4%	57.9%	0.169
FLOT [52]	LiDAR	—	—	34.3%	64.3%	0.156
FlowNet3D++ [89]	RGB-D	—	—	30.3%	63.4%	0.137
RAFT3D [13]	RGB-D	81.3%	2.43	82.1%	88.1%	0.064
ScaleRAFT3D (ours)	RGB-D	85.4%	2.02	85.4%	90.8%	0.049

TABLE V

ABLATION EXPERIMENTS. $Fl-epe$ IS THE END-TO-END OPTICAL FLOW ERROR, M_f IS THE NUMBER OF FLIGHT FOREGROUNDS.

Experiment	Method	M_f	r_s	$Fl-epe$	Mid_{error}
Scale Lookup Radius		0	0	3.52	160.63
		0	2/S	3.43	150.41
		0	1/S	3.47	147.92
Scale Feature	W/o F_{scale}	0	1/S	3.49	226.78
	W/o L_c^s	0	1/S	3.55	226.28
Hybrid Training Pipeline		1	1/S	3.28	129.53
		2	1/S	3.22	132.38
		3	1/S	3.45	139.31

F. Ablation

In this section, we conduct ablation experiments to further confirm the ScaleRAFT structure’s rationality. We train ScaleRAFT 280K iterations on Driving and Flyingthings3D, with batch = 6, lr = 0.00025, and conduct testing on K200. Our algorithm’s default configuration is $r_s = 1/S$, $M_f = 1$.

Scale Lookup Radius. The scale lookup radius specifies the sampling range of lookup operator L_c^s , but does not change the scale correlation feature’s dimension. Generally, when r_s is between $1/S$ and $2/S$, a slight change will not affect the final performance.

Scale Feature. We designed two ablation models to verify the effectiveness of scale lookup operator and scale correlation features.

In the “W/o F_{scale} ” model, we removed the scale correlation feature F_{scale} from the default model and only used optical flow correlation features F_{of} to predict the 3D flow. As shown in Tab. V, the performance of both optical flow and MID has significantly decreased, and the accuracy of 3D metrics has decreased more (147.92→226.78). It proves that scale correlation feature F_{scale} is essential in depth motion estimation.

In the “W/o L_c^s ” model, we do not use the scale lookup operator L_c^s , but directly use the F_{multi} for motion estimation in the depth direction. The experimental results show that the error of the ablation model is still larger than the default model, even if more features are used.

Hybrid Training Pipeline. We also tested the effect of different numbers of foreground flying objects on the training

results. As shown in Tab. V, when the current number of foregrounds is 1 and 2, performance significantly improved compared to the ground-truth training. When the current number of foregrounds reaches 3, the proportion of texture-matching learning exceeds regression learning, and the testing performance decreases.

TABLE VI

BREAKDOWN OF THE INFERENCE LATENCY. RESULTS ARE COMPUTED ON 1242x375 IMAGES WITH A RTX3090 GPU. THE INCREASED RUNNING TIME COMPARED TO THE BASELINE MODEL IS HIGHLIGHTED IN BOLD.

Models	Component	Individual Latency	Total Latency
ScaleRAFT	Feature extract	25ms (+20ms)	170.1ms
	Construct CSCV	0.8ms	
	Context extract	4.3ms	
	GRU update	128ms (+33ms)	
	Last f_3 update	12ms (+12ms)	
ScaleRAFT3D	Feature extract	21.9ms (+17.6ms)	289.7ms
	Construct CSCV	0.8ms	
	Resnet50	11ms	
	GRU update	216ms	
	$SE(3)$ update	40ms	

V. LATENCY AND LIMITATIONS

Latency. In Tab. VI, we provide the inference breakdown time on KITTI. The timing results were measured on RTX3090. We calculated the 1242x375 size image 200 times consecutively, taking the average time as the final latency. As we can see, the introduction of CSCV adds a total time of 65ms to the RAFT baseline, with 20ms used to extract additional multi-scale features and 45ms used to calculate motion in the depth direction. For the 3D flow baseline RAFT3D, the introduction of CSCV only increased the total time by 6.1% (17.6ms), which is spent on extracting multi-scale features. Note that we do not use acceleration technology like TensorRT⁴, so there is still room for optimization.

Limitations. Because ScaleRAFT needs to build a multi-scale cost volume, this increases memory usage from 3GB to 4.5GB compared to the RAFT baseline (only forward inference, with an input image size of 1242x375). Due to limited GPU memory, currently, we can only set the scale constant S to 4. In addition, the depth clues provided by our

⁴<https://github.com/NVIDIA/TensorRT>

ScaleRAFT are only accurate (error $< 5\%$) when the rotation speed is lower than $540^\circ/\text{s}$ (default 30FPS video input), and the depth motion estimation of high-speed rotating objects may fail. Therefore, our method is more suitable for driving scenarios with less rotation.

VI. CONCLUSION

In this article, we propose a new cross-scale recurrent all-pairs field transform for 3D motion estimation (ScaleRAFT), which extends the optical flow matching from the original image-to-image to image-to-scale-space, reducing the interference of scale changes on optical flow matching. Moreover, matching in scale space can also obtain depth motion clues, helping 3D flow methods break away from depth dependence and regression dependence. The comprehensive evaluation of different datasets shows that ScaleRAFT performs excellently in various 3D tasks, especially in areas with large scale changes. We hope this exciting result draws people to pay more attention to 3D motion estimation based on image feature matching.

VII. ACKNOWLEDGEMENT

We thank Professor Jiwen Lu of Tsinghua University for his constructive comments on this paper.

This research was supported by the National Natural Science Foundation of China (Grant nos. 61673220, 62106209, 62372235), and the Project of SongShan Laboratory (Grant no. YYJC012022015).

REFERENCES

- [1] Y. D. Yasuda, L. E. G. Martins, and F. A. Cappabianco, "Autonomous visual navigation for mobile robots: A systematic literature review," *ACM Computing Surveys*, vol. 53, no. 1, pp. 1–34, 2020.
- [2] L. Wang, H. Liu, S. Zhou, W. Tang, and G. Hua, "Instance motion tendency learning for video panoptic segmentation," *IEEE Transactions on Image Processing*, vol. 32, pp. 764–778, 2022.
- [3] P. Zhuang, Y. Guo, Z. Yu, L. Zhou, L. Bai, D. Liang, Z. Wang, Y. Wang, and W. Ouyang, "Action recognition with motion diversification and dynamic selection," *IEEE Transactions on Image Processing*, vol. 31, pp. 4884–4896, 2022.
- [4] Y. Kong and Y. Fu, "Human action recognition and prediction: A survey," *International Journal of Computer Vision*, vol. 130, no. 5, pp. 1366–1401, 2022.
- [5] A. Manglik, X. Weng, E. Ohn-Bar, and K. KITANI, "Future near-collision prediction from monocular video: Feasibility, dataset, and challenges," in *IEEE/RSJ International Conference on Intelligent Robots and Systems*, 2019.
- [6] D. N. Lee, "A theory of visual control of braking based on information about time-to-collision," *Perception*, vol. 5, no. 4, pp. 437–459, 1976.
- [7] J. Byrne and C. J. Taylor, "Expansion segmentation for visual collision detection and estimation," in *IEEE International Conference on Robotics and Automation*, 2009, pp. 875–882.
- [8] T. Marinho, M. Amrouche, V. Cichella, D. Stipanović, and N. Hovakimyan, "Guaranteed collision avoidance based on line-of-sight angle and time-to-collision," in *Annual American Control Conference*, 2018, pp. 4305–4310.
- [9] J. Zhang, J. Pan, D. Wang, S. Zhou, X. Wei, F. Zhao, J. Liu, and J. Ren, "Deep dynamic scene deblurring from optical flow," *IEEE Transactions on Circuits and Systems for Video Technology*, vol. 32, no. 12, pp. 8250–8260, 2021.
- [10] F. Guo, W. Wang, Z. Shen, J. Shen, L. Shao, and D. Tao, "Motion-aware rapid video saliency detection," *IEEE transactions on circuits and systems for video technology*, vol. 30, no. 12, pp. 4887–4898, 2019.
- [11] T. Yu, X. Lin, S. Wang, W. Sheng, Q. Huang, and J. Yu, "A comprehensive survey of 3d dense captioning: Localizing and describing objects in 3d scenes," *IEEE Transactions on Circuits and Systems for Video Technology*, vol. 34, no. 3, pp. 1322–1338, 2024.
- [12] J. Guo, J. Liu, and D. Xu, "3d-pruning: A model compression framework for efficient 3d action recognition," *IEEE Transactions on Circuits and Systems for Video Technology*, vol. 32, no. 12, pp. 8717–8729, 2022.
- [13] Z. Teed and J. Deng, "Raft-3d: Scene flow using rigid-motion embeddings," in *Proceedings of the IEEE/CVF Conference on Computer Vision and Pattern Recognition*, 2021, pp. 8375–8384.
- [14] H. Liu, T. Lu, Y. Xu, J. Liu, W. Li, and L. Chen, "Camliflow: bidirectional camera-lidar fusion for joint optical flow and scene flow estimation," in *Proceedings of the IEEE/CVF Conference on Computer Vision and Pattern Recognition*, 2022, pp. 5791–5801.
- [15] G. Yang and D. Ramanan, "Learning to segment rigid motions from two frames," in *Proceedings of the IEEE/CVF Conference on Computer Vision and Pattern Recognition*, 2021, pp. 1266–1275.
- [16] A. Behl, O. Hosseini Jafari, S. Karthik Mustikovela, H. Abu Alhaija, C. Rother, and A. Geiger, "Bounding boxes, segmentations and object coordinates: How important is recognition for 3d scene flow estimation in autonomous driving scenarios?" in *Proceedings of the IEEE/CVF International Conference on Computer Vision*, 2017, pp. 2574–2583.
- [17] W.-C. Ma, S. Wang, R. Hu, Y. Xiong, and R. Urtasun, "Deep rigid instance scene flow," in *Proceedings of the IEEE/CVF Conference on Computer Vision and Pattern Recognition*, 2019, pp. 3614–3622.
- [18] G. Yang and D. Ramanan, "Upgrading optical flow to 3d scene flow through optical expansion," in *Proceedings of the IEEE/CVF Conference on Computer Vision and Pattern Recognition*, 2020, pp. 1334–1343.
- [19] A. Badki, O. Gallo, J. Kautz, and P. Sen, "Binary ttc: A temporal geofence for autonomous navigation," in *Proceedings of the IEEE/CVF Conference on Computer Vision and Pattern Recognition*, 2021, pp. 12946–12955.
- [20] Z. Teed and J. Deng, "Raft: Recurrent all-pairs field transforms for optical flow," in *European Conference on Computer Vision*, 2020, pp. 402–419.
- [21] D. Sun, X. Yang, M.-Y. Liu, and J. Kautz, "Pwc-net: Cnns for optical flow using pyramid, warping, and cost volume," in *Proceedings of the IEEE/CVF Conference on Computer Vision and Pattern Recognition*, 2018, pp. 8934–8943.
- [22] T. Brox, A. Bruhn, N. Papenberg, and J. Weickert, "High accuracy optical flow estimation based on a theory for warping," in *European Conference on Computer Vision*, 2004, pp. 25–36.
- [23] N. Papenberg, A. Bruhn, T. Brox, S. Didas, and J. Weickert, "Highly accurate optic flow computation with theoretically justified warping," *International Journal of Computer Vision*, vol. 67, pp. 141–158, 2006.
- [24] T. Brox and J. Malik, "Large displacement optical flow: descriptor matching in variational motion estimation," *IEEE Transactions on Pattern Analysis and Machine Intelligence*, vol. 33, no. 3, pp. 500–513, 2010.
- [25] D. G. Lowe, "Distinctive image features from scale-invariant keypoints," *International Journal of Computer Vision*, vol. 60, pp. 91–110, 2004.
- [26] K. Mikolajczyk, T. Tuytelaars, C. Schmid, A. Zisserman, J. Matas, F. Schaffalitzky, T. Kadir, and L. V. Gool, "A comparison of affine region detectors," *International Journal of Computer Vision*, pp. 43–72, 2005.
- [27] M. Menze, C. Heipke, and A. Geiger, "Object scene flow," *ISPRS Journal of Photogrammetry and Remote Sensing*, vol. 140, pp. 60–76, 2018.
- [28] N. Mayer, E. Ilg, P. Hausser, P. Fischer, D. Cremers, A. Dosovitskiy, and T. Brox, "A large dataset to train convolutional networks for disparity, optical flow, and scene flow estimation," in *Proceedings of the IEEE/CVF conference on computer vision and pattern recognition*, 2016, pp. 4040–4048.
- [29] H. Ling, Q. Sun, Z. Ren, Y. Liu, H. Wang, and Z. Wang, "Scale-flow: Estimating 3d motion from video," in *Proceedings of the 30th ACM International Conference on Multimedia*, 2022, pp. 6530–6538.
- [30] D. Sun, S. Roth, J. Lewis, and M. J. Black, "Learning optical flow," in *European Conference on Computer Vision*, 2008, pp. 83–97.
- [31] B. K. Horn and B. G. Schunck, "Determining optical flow," *Artificial intelligence*, vol. 17, no. 1-3, pp. 185–203, 1981.
- [32] Y. Niu, A. Dick, and M. Brooks, "Compass rose: A rotational robust signature for optical flow computation," *IEEE transactions on circuits and systems for video technology*, vol. 24, no. 1, pp. 63–73, 2013.
- [33] Y. Li, E. Zhu, J. Zhao, J. Yin, and X. Zhao, "A fast simple optical flow computation approach based on the 3-d gradient," *IEEE transactions on circuits and systems for video technology*, vol. 24, no. 5, pp. 842–853, 2013.

- [34] S. Jiang, D. Campbell, Y. Lu, H. Li, and R. Hartley, "Learning to estimate hidden motions with global motion aggregation," in *Proceedings of the IEEE/CVF International Conference on Computer Vision*, 2021, pp. 9772–9781.
- [35] G. Yang and D. Ramanan, "Volumetric correspondence networks for optical flow," *Advances in neural information processing systems*, vol. 32, 2019.
- [36] A. Ranjan and M. J. Black, "Optical flow estimation using a spatial pyramid network," in *Proceedings of the IEEE/CVF Conference on Computer Vision and Pattern Recognition*, 2017, pp. 4161–4170.
- [37] Y. Lu, J. Valmadre, H. Wang, J. Kannala, M. Harandi, and P. Torr, "Devon: Deformable volume network for learning optical flow," in *Proceedings of the IEEE/CVF Winter Conference on Applications of Computer Vision*, 2020, pp. 2705–2713.
- [38] E. Ilg, N. Mayer, T. Saikia, M. Keuper, A. Dosovitskiy, and T. Brox, "FlowNet 2.0: Evolution of optical flow estimation with deep networks," in *Proceedings of the IEEE/CVF Conference on Computer Vision and Pattern Recognition*, 2017, pp. 2462–2470.
- [39] A. Dosovitskiy, P. Fischer, E. Ilg, P. Hausser, C. Hazirbas, V. Golkov, P. Van Der Smagt, D. Cremers, and T. Brox, "FlowNet: Learning optical flow with convolutional networks," in *Proceedings of the IEEE/CVF International Conference on Computer Vision*, 2015, pp. 2758–2766.
- [40] J. Chen, J. Lai, Z. Cai, X. Xie, and Z. Pan, "Optical flow estimation based on the frequency-domain regularization," *IEEE Transactions on Circuits and Systems for Video Technology*, vol. 31, no. 1, pp. 217–230, 2020.
- [41] Z. Liu, Z. Li, W. Chen, X. Wu, and Z. Liu, "Unsupervised optical flow estimation for differently exposed images in ldr domain," *IEEE Transactions on Circuits and Systems for Video Technology*, 2023.
- [42] J. Chen, Z. Cai, J. Lai, and X. Xie, "Efficient segmentation-based patchmatch for large displacement optical flow estimation," *IEEE Transactions on Circuits and Systems for Video Technology*, vol. 29, no. 12, pp. 3595–3607, 2018.
- [43] L. Kong and J. Yang, "Mdflow: Unsupervised optical flow learning by reliable mutual knowledge distillation," *IEEE Transactions on Circuits and Systems for Video Technology*, vol. 33, no. 2, pp. 677–688, 2022.
- [44] L. Xu, Z. Dai, and J. Jia, "Scale invariant optical flow," in *European Conference on Computer Vision*, 2012, pp. 385–399.
- [45] S. Wang, L. Luo, N. Zhang, and J. Li, "Autoscaler: scale-attention networks for visual correspondence," *arXiv preprint arXiv:1611.05837*, 2016.
- [46] S. Liu, K. Luo, A. Luo, C. Wang, F. Meng, and B. Zeng, "Asflow: Unsupervised optical flow learning with adaptive pyramid sampling," *IEEE Transactions on Circuits and Systems for Video Technology*, vol. 32, no. 7, pp. 4282–4295, 2021.
- [47] R. Zhao, R. Xiong, Z. Ding, X. Fan, J. Zhang, and T. Huang, "Mrdflow: Unsupervised optical flow estimation network with multi-scale recurrent decoder," *IEEE Transactions on Circuits and Systems for Video Technology*, vol. 32, no. 7, pp. 4639–4652, 2021.
- [48] M. Zhai, X. Xiang, R. Zhang, N. Lv, and A. El Saddik, "Optical flow estimation using dual self-attention pyramid networks," *IEEE Transactions on Circuits and Systems for Video Technology*, vol. 30, no. 10, pp. 3663–3674, 2019.
- [49] T. Senst, V. Eiselein, and T. Sikora, "Robust local optical flow for feature tracking," *IEEE Transactions on Circuits and Systems for Video Technology*, vol. 22, no. 9, pp. 1377–1387, 2012.
- [50] M. Menze and A. Geiger, "Object scene flow for autonomous vehicles," in *Proceedings of the IEEE/CVF Conference on Computer Vision and Pattern Recognition*, 2015, pp. 3061–3070.
- [51] C. Vogel, K. Schindler, and S. Roth, "3d scene flow estimation with a piecewise rigid scene model," *International Journal of Computer Vision*, pp. 1–28, 2015.
- [52] G. Puy, A. Boulch, and R. Marlet, "Flot: Scene flow on point clouds guided by optimal transport," in *European Conference on Computer Vision*, 2020, pp. 527–544.
- [53] X. Liu, C. R. Qi, and L. J. Guibas, "FlowNet3d: Learning scene flow in 3d point clouds," in *Proceedings of the IEEE/CVF Conference on Computer Vision and Pattern Recognition*, 2019, pp. 529–537.
- [54] Y. Wei, Z. Wang, Y. Rao, J. Lu, and J. Zhou, "Pv-raft: Point-voxel correlation fields for scene flow estimation of point clouds," in *Proceedings of the IEEE/CVF conference on computer vision and pattern recognition*, 2021, pp. 6954–6963.
- [55] W. Wu, Z. Qi, and F. P. Li, "Deep convolutional networks on 3d point clouds. ieec," in *Proceedings of the IEEE/CVF Conference on Computer Vision and Pattern Recognition*, 2019, pp. 9613–9622.
- [56] Z. Zhang, Y. Dai, B. Fan, J. Sun, and M. He, "Learning a task-specific descriptor for robust matching of 3d point clouds," *IEEE Transactions on Circuits and Systems for Video Technology*, vol. 32, no. 12, pp. 8462–8475, 2022.
- [57] X. Huang, J. Zhang, Q. Wu, L. Fan, and C. Yuan, "A coarse-to-fine algorithm for matching and registration in 3d cross-source point clouds," *IEEE Transactions on Circuits and Systems for Video Technology*, vol. 28, no. 10, pp. 2965–2977, 2017.
- [58] Z. Zhang, J. Sun, Y. Dai, B. Fan, and M. He, "Vrnet: Learning the rectified virtual corresponding points for 3d point cloud registration," *IEEE Transactions on Circuits and Systems for Video Technology*, vol. 32, no. 8, pp. 4997–5010, 2022.
- [59] S. Ren, Y. Zeng, J. Hou, and X. Chen, "Corri2p: Deep image-to-point cloud registration via dense correspondence," *IEEE Transactions on Circuits and Systems for Video Technology*, vol. 33, pp. 1198–1208, 2022.
- [60] H. Shi, R. Li, F. Liu, and G. Lin, "Temporal feature matching and propagation for semantic segmentation on 3d point cloud sequences," *IEEE Transactions on Circuits and Systems for Video Technology*, vol. 33, no. 12, pp. 7491–7502, 2023.
- [61] P. An, X. Hu, J. Ding, J. Zhang, J. Ma, Y. Yang, and Q. Liu, "Ol-reg: Registration of image and sparse lidar point cloud with object-level dense correspondences," *IEEE Transactions on Circuits and Systems for Video Technology*, pp. 1–1, 2024.
- [62] T. Camus, "Calculating time-to-contact using real-time quantized optical flow," *Nation Institute of Standards and Technology Nistir*, 1995.
- [63] D. Muller, J. Pauli, C. Nunn, S. Gormer, and S. Muller-Schneiders, "Time to contact estimation using interest points," in *12th International IEEE Conference on Intelligent Transportation Systems*, 2009, pp. 1–6.
- [64] M. Sagrebin, A. Noglik, and J. Pauli, "Robust time-to-contact calculation for real time applications," in *Proc. of 18th International Conference on Computer Graphics and Vision*, 2008, pp. 128–133.
- [65] J. Chao, R. Huitl, E. Steinbach, and D. Schroeder, "A novel rate control framework for sift/surf feature preservation in h. 264/avc video compression," *IEEE Transactions on Circuits and Systems for Video Technology*, vol. 25, no. 6, pp. 958–972, 2014.
- [66] J.-S. Park, H.-E. Kim, H.-Y. Kim, J. Lee, and L.-S. Kim, "A vision processor with a unified interest-point detection and matching hardware for accelerating a stereo-matching algorithm," *IEEE Transactions on Circuits and Systems for Video Technology*, vol. 26, no. 12, pp. 2328–2343, 2015.
- [67] Y. Lei, W. Luo, Y. Wang, and J. Huang, "Video sequence matching based on the invariance of color correlation," *IEEE transactions on circuits and systems for video technology*, vol. 22, no. 9, pp. 1332–1343, 2012.
- [68] J. Dong, M. Hu, J. Lu, and S. Han, "Affine template matching based on multi-scale dense structure principal direction," *IEEE Transactions on Circuits and Systems for Video Technology*, vol. 31, no. 6, pp. 2125–2132, 2020.
- [69] Y. Li, F. Wang, R. Stevenson, R. Fan, and H. Tan, "Reliable line segment matching for multispectral images guided by intersection matches," *IEEE Transactions on Circuits and Systems for Video Technology*, vol. 29, no. 10, pp. 2899–2912, 2018.
- [70] C. Henderson and E. Izquierdo, "Robust feature matching in long-running poor-quality videos," *IEEE Transactions on Circuits and Systems for Video Technology*, vol. 26, no. 6, pp. 1161–1174, 2016.
- [71] S. Khan, M. Nawaz, X. Guoxia, and H. Yan, "Image correspondence with cur decomposition-based graph completion and matching," *IEEE Transactions on Circuits and Systems for Video Technology*, vol. 30, no. 9, pp. 3054–3067, 2019.
- [72] X. Dong, J. Shen, and L. Shao, "Hierarchical superpixel-to-pixel dense matching," *IEEE Transactions on Circuits and Systems for Video Technology*, vol. 27, no. 12, pp. 2518–2526, 2016.
- [73] G. Yammine, E. Wige, F. Simmet, D. Niederkorn, and A. Kaup, "Novel similarity-invariant line descriptor and matching algorithm for global motion estimation," *IEEE transactions on circuits and systems for video technology*, vol. 24, no. 8, pp. 1323–1335, 2014.
- [74] J. Lu and Z. Lin, "Deliberation with "fast full-search block matching"," *IEEE Transactions on Circuits and Systems for Video Technology*, vol. 13, no. 1, pp. 97–99, 2003.
- [75] M. Liu and T. Delbruck, "Edflow: Event driven optical flow camera with keypoint detection and adaptive block matching," *IEEE Transactions on Circuits and Systems for Video Technology*, vol. 32, no. 9, pp. 5776–5789, 2022.
- [76] T. Lindeberg, "Feature detection with automatic scale selection," *International Journal of Computer Vision*, pp. 79–116, 1998.
- [77] D. Sun, C. Herrmann, F. Reda, M. Rubinstein, D. J. Fleet, and W. T. Freeman, "Disentangling architecture and training for optical flow," in *European Conference on Computer Vision*. Springer, 2022, pp. 165–182.

- [78] H. Zhao, J. Shi, X. Qi, X. Wang, and J. Jia, "Pyramid scene parsing network," in *Proceedings of the IEEE/CVF conference on computer vision and pattern recognition*, 2017, pp. 2881–2890.
- [79] H. Pan, Y. Hong, W. Sun, and Y. Jia, "Deep dual-resolution networks for real-time and accurate semantic segmentation of traffic scenes," *IEEE Transactions on Intelligent Transportation Systems*, vol. 24, no. 3, pp. 3448–3460, 2022.
- [80] J. A. Hesch and S. I. Roumeliotis, "A direct least-squares (dls) method for pnp," in *International Conference on Computer Vision (ICCV)*. IEEE, 2011, pp. 383–390.
- [81] V. Lepetit, F. Moreno-Noguer, and P. Fua, "Ep n p: An accurate o (n) solution to the p n p problem," *International journal of computer vision (IJCV)*, vol. 81, pp. 155–166, 2009.
- [82] K. He, X. Zhang, S. Ren, and J. Sun, "Deep residual learning for image recognition," in *Proceedings of the IEEE/CVF Conference on Computer Vision and Pattern Recognition*, 2016, pp. 770–778.
- [83] D. J. Butler, J. Wulff, G. B. Stanley, and M. J. Black, "A naturalistic open source movie for optical flow evaluation," in *European Conference on Computer Vision*, 2012, pp. 611–625.
- [84] J. Hur and S. Roth, "Self-supervised monocular scene flow estimation," in *Proceedings of the IEEE/CVF Conference on Computer Vision and Pattern Recognition*, 2020, pp. 7396–7405.
- [85] J. Lambert, Z. Liu, O. Sener, J. Hays, and V. Koltun, "Mseg: A composite dataset for multi-domain semantic segmentation," in *Proceedings of the IEEE/CVF conference on computer vision and pattern recognition*, 2020, pp. 2879–2888.
- [86] H. Ling, Y. Sun, Q. Sun, and Z. Ren, "Learning optical expansion from scale matching," in *Proceedings of the IEEE/CVF Conference on Computer Vision and Pattern Recognition*, 2023, pp. 5445–5454.
- [87] T. Mori and S. Scherer, "First results in detecting and avoiding frontal obstacles from a monocular camera for micro unmanned aerial vehicles," in *IEEE International Conference on Robotics and Automation*, 2013, pp. 1750–1757.
- [88] F. Zhang, V. Prisacariu, R. Yang, and P. H. Torr, "Ga-net: Guided aggregation net for end-to-end stereo matching," in *Proceedings of the IEEE/CVF Conference on Computer Vision and Pattern Recognition*, 2019, pp. 185–194.
- [89] Z. Wang, S. Li, H. Howard-Jenkins, V. Prisacariu, and M. Chen, "Flownet3d++: Geometric losses for deep scene flow estimation," in *Proceedings of the IEEE/CVF winter conference on applications of computer vision*, 2020, pp. 91–98.